

<https://doi.org/10.1038/s44306-025-00072-5>

Single-shot electrical detection of short-wavelength magnon pulse transmission in a magnonic thin-film waveguide

Check for updates

Moojune Song^{1,2}, Jinho Lim³, Wei Zhang⁴, Dmytro A. Bozhko⁵, Ralu Divan⁶, Axel Hoffmann³✉, Kab-Jin Kim²✉, Valentine Novosad¹✉ & Yi Li¹✉

The advance of magnon spintronics requires understanding of time-domain magnon pulse transmission in order to develop high-speed information processing protocols. In this work, we demonstrate single-shot electrical detection of narrow-band magnon pulse transmission in a yttrium iron garnet thin-film delay line. The high signal-to-background ratio of magnon transmission band allows us to directly probe the magnon transmission electrically using a fast oscilloscope and to study its spectral evolution using Fast Fourier Transform (FFT) of the time-domain transmitted signal. At elevated input power, we show a magnon transmission reduction and a spectral distortion, which can be understood by the nonlinear magnon excitation in the transmission band defined by the antenna geometry. In addition, we also find that the higher- (lower-) frequency magnon spectral component exhibits a lower (higher) magnon group velocity, showing a dispersion agreeing with the Damon-Eshbach dependence. Our results provide important guidance of magnon pulse engineering for their applications in spin wave computing and coherent magnon information processing.

Magnonics provides a different degree of freedom beyond electron transport for information transfer and processing^{1–6}. Because magnons carry both amplitude and phase information, they can be utilized for wave-based coherent information processing and logic operations. In addition, because of the unique dispersion relationship due to magnetic dipolar and exchange interactions⁷, magnon excitations can achieve short wavelength below 1 μm while in the gigahertz frequency regime. Thus, they provide opportunities for miniaturizing microwave circuits and breaking the physical limitation of microwave components⁸, with many recent works demonstrating the functionality of magnonics in the sub-micron length scale for both the magnon conduit dimension and the magnon wavelength^{9–13}.

One classical magnon-microwave transducer architecture is the magnon delay line, which has been widely used for implementing magnonic device concepts such as logic gate^{14–18}, phase shifter^{19,20} and multiplexer^{21–24}. Nevertheless, most works were done with continuous-wave (CW) magnon excitations²⁵. In order to cultivate the potential of high-speed information processing with magnonics, it is essential to understand the real-time transmission properties of narrow-band magnon pulses besides CW excitations²⁶. This is because magnons exhibit highly nonlinear $\omega - k$

dispersion relationship and their propagation can easily lead to temporal and spectral distortion and thus the loss of information. Up to now, most studies of short-width pulse magnon propagation have been focusing on optical detection such as microfocused Brillouin light scattering (μ -BLS)^{10,27–30}, which is challenging as a detector for integrated circuits. In addition, because of the fundamental limitation in scattering cross section with μ -BLS, the temporal studies of magnon transmission will inevitably require signal accumulation over thousands of events^{28,31,32}. This can cause measurement inaccuracy due to phase slip from both ambient noise and pulse modulation, and slow down the logic operation speed with long integration time.

In this work, we conduct single-shot electric detection of pulse magnon transmission in a yttrium iron garnet (YIG) thin film delay line with short pulse width, narrow bandwidth, and short wavelength. We focus on magnon pulse with a single carrier frequency, which is generated by mixing a CW microwave with a square voltage pulse [Fig. 1a]. This is advantageous for studying magnon dispersion and nonlinear properties over previous broad-spectrum pulse voltage excitations^{33–35}. The time- and frequency-domain evolutions of the magnon pulses can be measured using a

¹Materials Science Division, Argonne National Laboratory, Lemont, IL, 60439, USA. ²Department of Physics, Korea Advanced Institute of Science and Technology, Daejeon, 34141, Republic of Korea. ³Department of Materials Science and Engineering and Materials Research Laboratory, The Grainger College of Engineering, University of Illinois Urbana-Champaign, Urbana, IL, 61820, USA. ⁴Department of Physics and Astronomy, University of North Carolina, Chapel Hill, NC, 27599, USA. ⁵Department of Physics and Energy Science, University of Colorado Colorado Springs, Colorado Springs, CO, 80918, USA. ⁶Center for Nanoscale Materials, Argonne National Laboratory, Argonne, IL, 60439, USA. ✉e-mail: axelh@illinois.edu; kabjin@kaist.ac.kr; novosad@anl.gov; yili@anl.gov

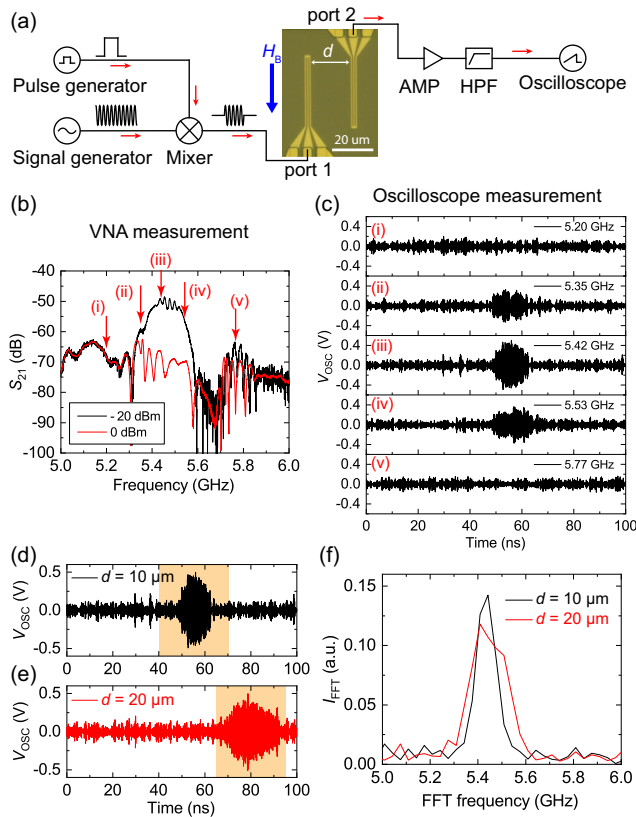


Fig. 1 | Schematic of electrical detection of short-wavelength magnon pulse transmission and the transmission characteristics. **a** Schematic of electrical detection of short-wavelength magnon pulse transmission in a YIG delay line, with an in-plane magnetic field H_B parallel to the CPW direction. The optical microscope picture shows a pair of CPWs with a length of $30\ \mu\text{m}$ and a separation of $d = 20\ \mu\text{m}$. **b** VNA measurements of power density spectrum for the device shown in **(a)** at $\mu_0 H_B = 0.11\ \text{T}$, with the magnon propagation direction from port 1 to port 2. **c** Oscilloscope measurements of time traces of a 10 ns microwave pulse excitation at different carrier frequencies, with the same condition in **(b)**. **d, e** Comparison of time traces between **(d)** $d = 10\ \mu\text{m}$ and **(e)** $d = 20\ \mu\text{m}$ with a pulse carrier frequency of $\omega_c/2\pi = 5.42\ \text{GHz}$. **f** FFT of **(d)** and **(e)**.

high-frequency oscilloscope and by conducting fast-Fourier transform (FFT) of the signals, yielding important information about their nonlinear behaviors in the temporal and spectral dimensions. With increased excitation power, we show that the transmitted pulse signal experiences an amplitude saturation and reduction along with an interesting spectral distortion in the FFT analysis, suggesting a nonlinear four-wave mixing process in the magnon state due to Suhl instability³⁶. In the temporal profile, we show that different frequency components in a magnon pulse can be separated temporally due to their difference in group velocity. Our work reveals important time- and frequency-domain properties and nonlinear effect of magnon pulse signal transmission for designing future high-data-rate magnonic circuits.

The YIG delay line was fabricated using a 100 nm-thick YIG film grown on gadolinium gallium garnet (GGG) substrate by liquid phase epitaxy (LPE). A pair of parallel ground-signal-ground (GSG) coplanar waveguide (CPW) antennas with Ti(5 nm)/Au(50 nm) electrodes were fabricated on the YIG pattern by E-beam lithography for magnon excitation. The total length of the antennas are $30\ \mu\text{m}$ and their separation is $d = 10$ or $20\ \mu\text{m}$. The three electrodes of each GSG antennas and their gaps have an equal width of 500 nm, leading to a maximal coupling efficiency to magnon wavelength of $\sim 2\ \mu\text{m}$ ³⁷. More details about the YIG delay line can be found in ref. 13. Figure 1a shows the diagram of the measurement circuit. A pulse generator is used to generate a square voltage pulse with a width of $\tau = 4, 7$ or 10 ns, which is then sent to a mixer for microwave pulse generation. In order to perform single-shot magnon pulse measurements, we use two 30 dB low-

noise amplifiers connected in series, followed by a high-pass filter over 4.5 GHz to minimize low-frequency thermal noise.

Figure 1b shows the microwave transmission spectrum for the delay line with $d = 20\ \mu\text{m}$ measured by a vector network analyzer (VNA), with an external field of $\mu_0 H_B = 0.11\ \text{T}$ applying parallel to the CPW direction. Note that the VNA data are without background subtraction. Under this condition, Damon-Eshbach magnetostatic spin wave mode will be excited with the major transmission direction from port 1 to 2, i.e. $\vec{k} \parallel \hat{n} \times \vec{M}$ where \hat{n} is the surface normal and \vec{M} is the magnetization direction [Fig. 1a]. In this work, we only work with this magnon propagating direction in order to maximize signal-to-background ratio³⁸. With an input power of $-20\ \text{dBm}$, a plateau of magnon transmission band is centered at 5.42 GHz with a 3 dB bandwidth of around 0.15 GHz. We highlight that the device exhibits a spin wave transmission band which is 20 dB higher than the background. This ensures a dominating magnon signal in the time-domain measurements over the background radiation transmission, which is essential for obtaining low-noise spectral analysis. As the input power is increased to 0 dBm, well above the CW nonlinearity threshold power of $-15\ \text{dBm}$ as determined from separate experiments, the plateau is flattened due to the nonlinear magnon scattering. However, because the VNA measurements only probe the response within a limited bandwidth, additional information about nonlinear effects such as frequency broadening and temporal dispersion of a single-frequency pulse input is missing. These characteristics can be probed by real-time magnon pulse transmission measurements.

The measured single-shot, time-domain magnon transmission traces are shown in Figure 1(c) from a 10-ns microwave pulse excitation at different carrier frequencies. The excitation microwave power is $P_c = -5\ \text{dBm}$ and in the linear excitation regime. As will be shown in the following measurements, the nonlinearity threshold for the 10-ns pulse microwave excitation is around $+5\ \text{dBm}$, which is much higher than the CW nonlinearity threshold because CW excitation injects more energy with a longer duration. When the carrier frequency is at (ii) 5.35 GHz, (iii) 5.42 GHz, and (iv) 5.53 GHz which are within the magnon transmission band in Fig. 1b, a strong wave packet is observed at around $t = 55\ \text{ns}$. It corresponds to the signal transmitted by magnons due to the long delay time from the trigger at $t = 0\ \text{ns}$. The magnon transmission wave packet is missing when the carrier frequency is off the transmission band at (i) 5.20 GHz and (v) 5.77 GHz. Due to the nonzero microwave propagation time in the cables, the trigger time of the oscilloscope does not match with the magnon excitation time at port 1. Thus, the most accurate way to measure the magnon propagation time is to compare the time delay with different CPW separation distances. Figure 1d, e compare the traces for $d = 10$ and $20\ \mu\text{m}$ with a pulse excitation of $\omega_c/2\pi = 5.42\ \text{GHz}$. The temporal broadening of the magnon wave packet from $d = 10\ \mu\text{m}$ to $20\ \mu\text{m}$ is attributed to the group velocity dispersion at different frequencies¹³, which can be compensated by exciting the magnons at a flat dispersion regime between the dipolar and exchange spin wave limits²⁷. The magnon signals show a time delay of 25 ns, which yields a group velocity of $v_g = 400\ \text{m/s}$. This value matches well with our previous reported group velocity of $v_g = 208\ \text{m/s}$ at 10 GHz measured in the same device with CW measurements¹³. Since in the long-wavelength limit v_g is inversely proportional to frequency, the expected group velocity should be $208 \times 10/5.42 = 384\ \text{m/s}$, close to the experimental result above. Figure 1f shows the FFT spectra of the traces in (d) and (e). We note that for $d = 20\ \mu\text{m}$ the FFT linewidth is slightly broader than for $d = 10\ \mu\text{m}$, which may be a consequence of additional noise during magnon wave packet propagation.

Figure 2 compares the temporal traces and their FFT spectra before and after passing through the YIG delay line. The microwave pulse generated by the mixer shows a sharp edge of amplitude modulation [Fig. 2a] by the square pulse. Its FFT spectrum shows a typical multi-peak characteristic of a square pulse with the center frequency defined by the microwave carrier frequency ω_c , as shown in Fig. 2(c). After the YIG delay line, the temporal trace is broadened and rounded, as shown in Fig. 2b. This is the result of narrow-band filtering by the antenna-defined magnon transmission band, as well as nonlinear $v_g - \omega$ magnon dispersion. The FFT of transmitted magnon wave packet shown in Fig. 2d matches well with the magnon transmission band measured by VNA in Fig. 1b.

Fig. 2 | Comparison of time traces before and after YIG delay line filtering with $d = 10 \mu\text{m}$, $\tau = 10 \text{ ns}$, $P_c = -5 \text{ dBm}$ and at $\mu_0 H_B = 0.11 \text{ T}$. **a** Microwave pulse with a carrier frequency of $\omega_c/2\pi = 5.42 \text{ GHz}$. **b** The same pulse in (a) after going through the YIG delay line and being amplified and filtered. **c** FFT of (a) measured at different ω_c . **d** FFT of (b) measured at different ω_c .

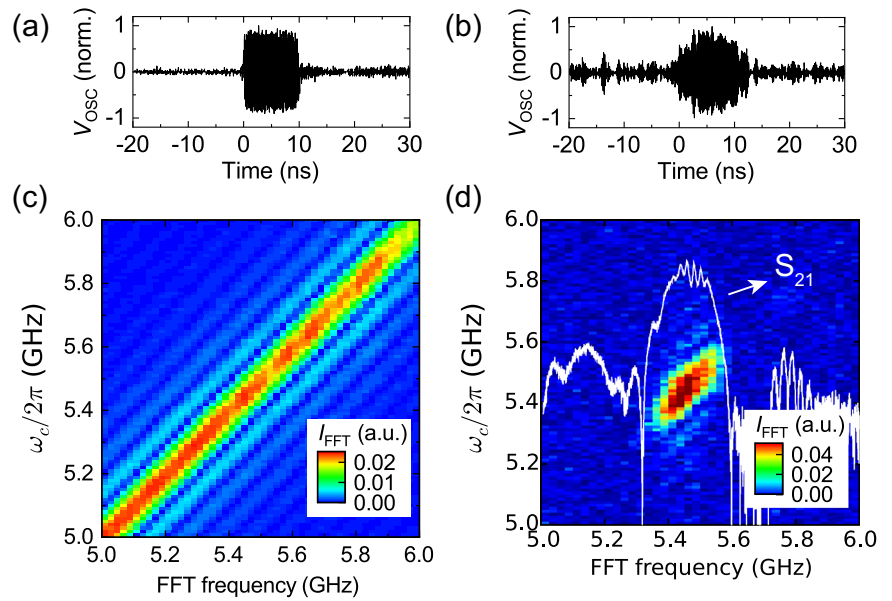
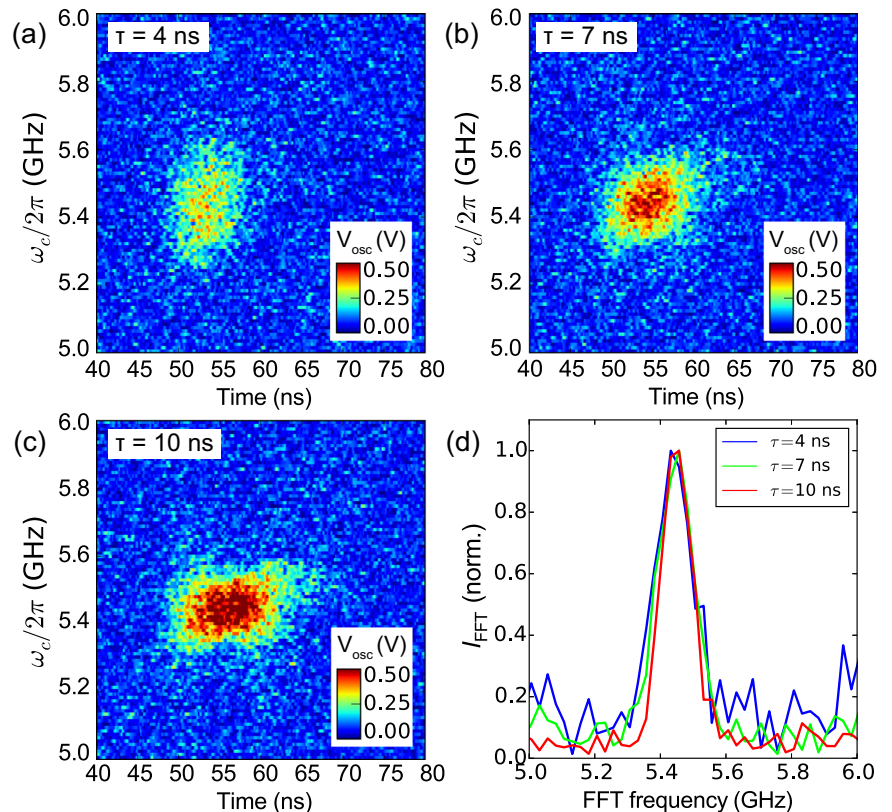


Fig. 3 | Comparison of time traces with different pulse widths. **a** $\tau = 4 \text{ ns}$; **b** $\tau = 7 \text{ ns}$; **c** $\tau = 10 \text{ ns}$. Dashed rectangles mark the expected pulse width τ and frequency bandwidth $1/\tau$, as (a) 4 ns and 250 MHz, (b) 7 ns and 143 MHz, and (c) 10 ns and 100 MHz, respectively. **d** Comparison of normalized FFT of temporal traces from (a–c) at $\omega_c/2\pi = 5.42 \text{ GHz}$.



Next, we move to the mapping of temporal traces measured at various carrier frequencies of the excitation microwave (ω_c , y -axis). Figure 3a–c compare the temporal traces of transmitted microwave pulses with different pulse widths at $d = 10 \mu\text{m}$. For $\tau = 4, 7$ and 10 ns , the temporal widths of the measured pulse (x -axis) matches with τ , showing that the pulse width is conserved within a small magnon propagation distance. However, we point out that the pulse width is broadened as magnon propagates, which is measured in Fig. 1e at $d = 20 \mu\text{m}$. Similar phenomenon has also been observed in μ -BLS measurements²⁷. In addition, at $\tau = 4 \text{ ns}$ the signal-obtaining excitation frequency bandwidth (y -axis) becomes broader than the allowed magnon transmission bandwidth of 150 MHz in Fig. 1b. This is

because the FFT bandwidth of the microwave pulse, which is inversely proportional to the pulse width as $1/\tau = 250 \text{ MHz}$, becomes significantly larger than the magnon transmission bandwidth, whereas for $\tau = 7$ or 10 ns the FFT bandwidth is within the magnon bandwidth. Despite the temporal pulse distortion at different τ , their FFT frequency spectra are consistent in terms of center frequency and linewidth, as shown in Fig. 3d for $\omega_c = 5.42 \text{ GHz}$. Thus, we conclude that the spectral property of magnon pulses are robust against pulse width, but will eventually scatter as the traveling distance increases due to intrinsic nonlinear dispersion property.

In order to explore the nonlinear behaviors of pulse magnon transmission, we conduct time-domain measurements at $\tau = 10 \text{ ns}$ with different

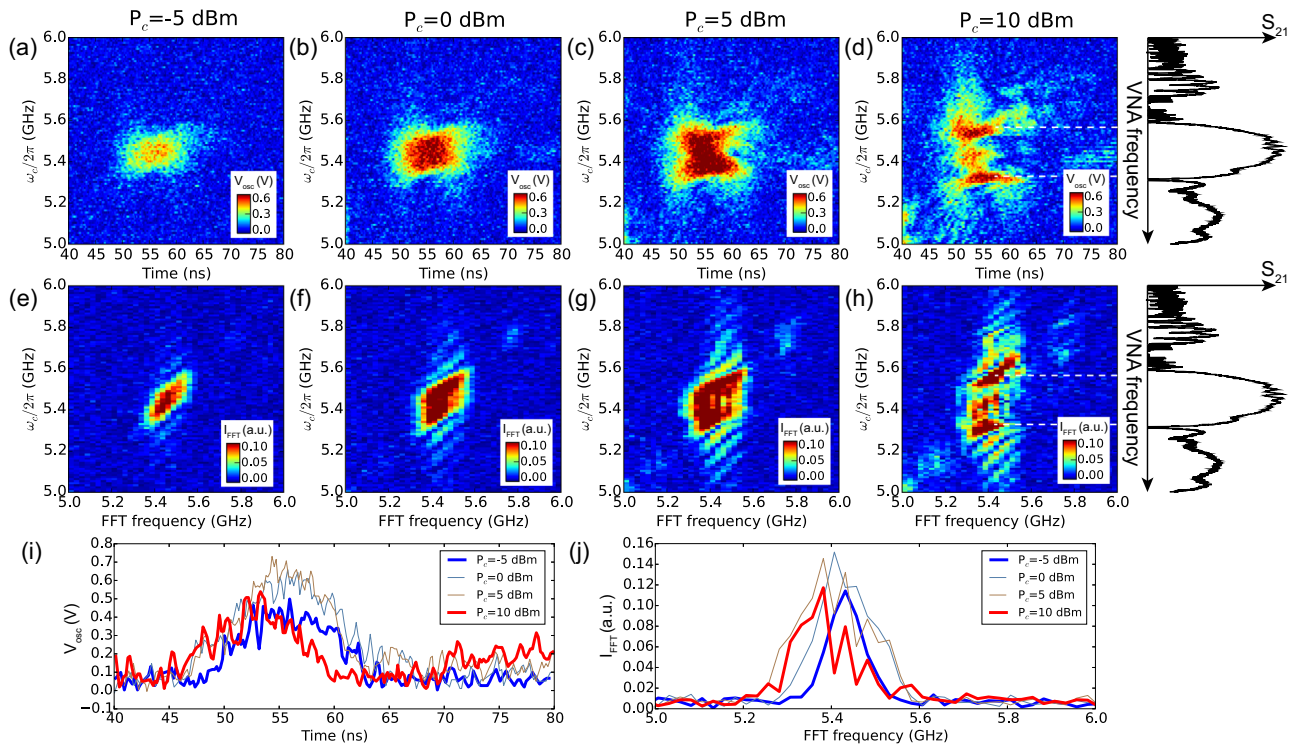


Fig. 4 | Power-dependent evolution of pulse magnon transmission in the time domain and frequency domain with $d = 10 \mu\text{m}$, $\tau = 10 \text{ ns}$, and at $\mu_0 H_B = 0.11 \text{ T}$. a–d Time-domain traces as a function of carrier frequency ω_c at (a) $P_c = -5 \text{ dBm}$, (b) $P_c = 0 \text{ dBm}$, (c) $P_c = 5 \text{ dBm}$, and (d) $P_c = 10 \text{ dBm}$. e–h FFT of (a–d) at different

powers. The wide dashed lines in (b, c, f, g) are separately analyzed in Fig. 4. i Upper envelopes of the temporal traces of pulse magnon transmission from (a–d) at $\omega_c/2\pi = 5.42 \text{ GHz}$, with $P_c = -5 \text{ dBm}$ and 10 dBm highlighted in blue and red colors, respectively. j FFT of the time traces in (i).

carrier microwave powers P_c with the upper envelopes of the measured wave packets V_{osc}^{max} shown in Fig. 4a–d. As P_c increases, the amplitude first increases from $P_c = -5 \text{ dBm}$ to $P_c = 0 \text{ dBm}$, then maintains the same level up to $P_c = 5 \text{ dBm}$, and eventually starts to decrease at $P_c = 10 \text{ dBm}$. This amplitude evolution is shown in Fig. 4i by comparing V_{osc}^{max} at $\omega_c/2\pi = 5.42 \text{ GHz}$. The measured V_{osc}^{max} at $P_c = 10 \text{ dBm}$ (red) is clearly smaller than $P_c = 0$ and 5 dBm , showing that the total transmitted signal is decreased at large P_c . The amplitude reduction at large P_c is accompanied with a broad expansion of the frequency bandwidth along the ω_c axis, which is also shown in the FFT spectra in Fig. 4e–h. We note that in Fig. 4d the amplitude reduction mainly happens around $\omega_c/2\pi = 5.4 \text{ GHz}$ where the magnon transmission efficiency is the highest. As ω_c moves to the edges of the VNA-measured magnon transmission band around 5.3 and 5.5 GHz , which are marked by the white dashed lines, the measured temporal pulse trace returns back to high amplitude.

The above observation of amplitude change can be explained by the Suhl instability of magnons with clear evidence of four-wave mixing process as shown by the broadening of the FFT spectra. In particular, the amplitude recurrence in Fig. 4d happens at the edge of the magnon transmission band, as compared with the S_{21} transmission band to the right. As shown in Fig. 4i, this is because V_{osc} is maximized for $P_c = 0$ and 5 dBm , and becomes weaker for either higher or lower powers. In Fig. 4d, because of the transmission efficiency, only at the edges does the power stay at the sweet zone in Fig. 4i and that's where V_{osc} shows a maximal value. Nonlinear magnonic phenomena have been widely observed in the CW BLS measurements^{39–41} or electrical measurements^{42,43}. Besides four-wave mixing, a three-magnon-mixing induced magnon confluence process may also involve^{44–48}. In our device geometry, because the detecting CPW is spatially separated from the excitation CPW, it is possible that the nonlinear magnon excitations are either dissipated locally at the excitation antenna, or has a much slower group velocity and cannot propagate to the detecting antenna. The amplitude reduction can be also observed in the FFT spectra, where the intensity around $\omega_c/2\pi = 5.4 \text{ GHz}$ at $P_c = 10 \text{ dBm}$ [Fig. 4h] is weaker than the intensity

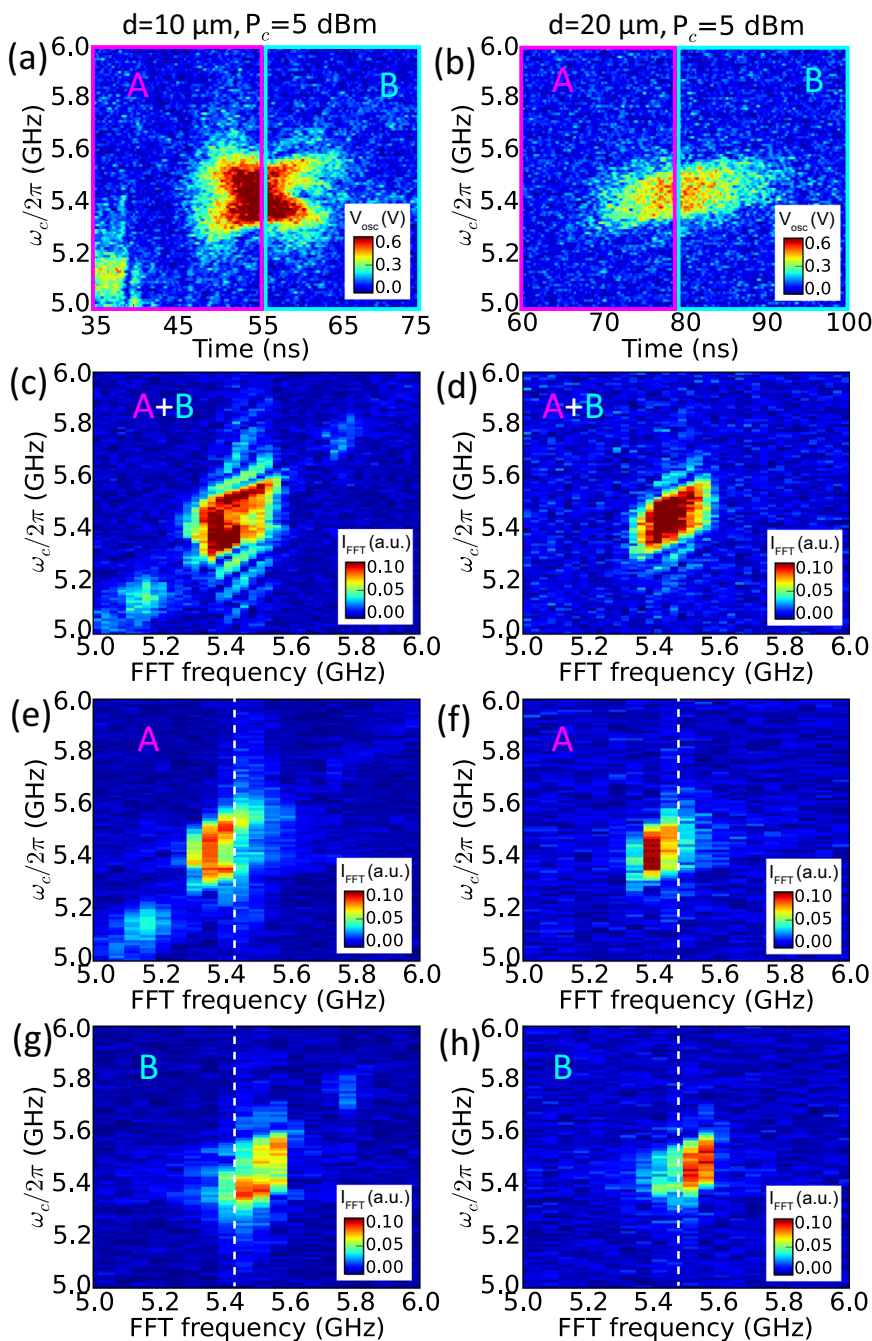
at $P_c = 0$ and 5 dBm [Fig. 4f, g], also compared in Fig. 4j. In addition, we also note that despite the frequency bandwidth broadening along the ω_c axis (y-axis) in Fig. 4e–h, the frequency bandwidth of the FFT spectra (x-axis) is always filtered by the magnon transmission band, which is determined by the CPW geometry and independent of P_c .

Finally, we show evidence of group velocity dispersion from the FFT spectral analysis. Figure 5a, b show the temporal traces for the YIG delay lines for $\tau = 10 \text{ ns}$ with $d = 10 \mu\text{m}$ and $20 \mu\text{m}$, respectively, with their FFT spectra shown in Fig. 5c, d. As discussed before, the temporal width of the transmitted wave packet is broadened from $d = 10 \mu\text{m}$ to $d = 20 \mu\text{m}$ even though their frequency bandwidths are similar, which suggests group velocity dispersion at different frequencies. To further demonstrate the spectral dispersion, we divide the temporal traces in two halves as shown by the magenta (A) and cyan (B) boxes in Fig. 5a, b, and show the FFT spectra for each regime in Fig. 5e–h. The FFT spectra of regime A and B correspond to the lower- and higher-frequency regimes of the total spectrum (A + B), respectively. This also shows that the higher-frequency magnon component exhibit a lower magnon group velocity because it takes longer time for this wave packet component to propagate to the detecting antenna [regime B in Fig. 5a, b], agreeing with the Damon-Eshbach magnon dispersion⁷. The observation of FFT spectral separation holds for all τ , P_c , and d , showing a robust group velocity dispersion of magnon against different device parameters.

Discussion

Our demonstration of single-shot time-domain electrical measurements of magnon pulse transmission allow us to access its temporal and spectral characteristics in a realistic magnon delay line device, and to study the device performance for future high-speed spintronic operations. Particularly, our study reveals two interesting properties in magnon pulse transmission. The first is the nonlinear pulse amplitude saturation and suppression at large excitation powers. The second is that different sections of temporal traces lead to different FFT spectra, which is due to group velocity dispersion of

Fig. 5 | FFT spectra for different temporal regimes.
a, b Temporal traces as a function of ω_c for (a) $d = 10 \mu\text{m}$ and (b) $d = 20 \mu\text{m}$, with $\tau = 10 \text{ ns}$. The boxes separate the temporal traces into two regimes (A and B) from the center of the traces, at (a) $t = 56 \text{ ns}$ and (b) $t = 79 \text{ ns}$. **c, d** FFT of the entire time regime in (a, b) (A + B). **e, f** FFT of regime A in (a, b). **g-h** FFT of regime B in (a, b).



magnons. Our results show that magnon pulse transmission is a highly nonlinear process due to the unique magnon frequency-wavelength dispersion relationship and nonlinear magnon scattering process, which are important for being considered in real-time magnon-based information processing such as logic gate^{15,17} and quantum information⁴⁹.

Data Availability

No datasets were generated or analysed during the current study.

Received: 18 September 2024; Accepted: 21 January 2025;

Published online: 01 April 2025

References

1. Kruglyak, V. V., Demokritov, S. O. & Grundler, D. Magnonics. *J. Phys. D: Appl. Phys.* **43**, 264001 (2010).
2. Serga, A. A., Chumak, A. V. & Hillebrands, B. Yig magnonics. *J. Phys. D: Appl. Phys.* **43**, 264002 (2010).
3. Chumak, A. V., Vasyuchka, V. I., Serga, A. A. & Hillebrands, B. Magnon spintronics. *Nature Phys.* **11**, 453 (2015).
4. Mahmoud, A. et al. Introduction to spin wave computing. *J. Appl. Phys.* **128**, 161101 (2020).
5. Barman, A. et al. The 2021 magnonics roadmap. *J. Phys.: Cond. Matter* **33**, 413001 (2021).
6. Flebus, B. et al. The 2024 magnonics roadmap. *J. Phys.: Cond. Matter* **36**, 363501 (2024).
7. Demokritov, S., Hillebrands, B. & Slavin, A. Brillouin light scattering studies of confined spin waves: linear and nonlinear confinement. *Phys. Rep.* **348**, 441–489 (2001).
8. Wang, Q., Csaba, G., Verba, R., Chumak, A. V. & Pirro, P. Nanoscale magnonic networks. *Phys. Rev. Appl.* **21**, 040503 (2024).

9. Liu, C. et al. Long-distance propagation of short-wavelength spin waves. *Nat. Commun.* **9**, 738 (2018).
10. Heinz, B. et al. Propagation of spin-wave packets in individual nanosized yttrium iron garnet magnonic conduits. *Nano Lett.* **20**, 4220–4227 (2020).
11. Baumgaertl, K. et al. Nanoimaging of ultrashort magnon emission by ferromagnetic grating couplers at GHz frequencies. *Nano. Lett.* **20**, 7281 (2020).
12. Inman, J. et al. Hybrid magnonics for short-wavelength spin waves facilitated by a magnetic heterostructure. *Phys. Rev. Appl.* **17**, 044034 (2022).
13. Li, Y. et al. Unidirectional microwave transduction with chirality selected short-wavelength magnon excitations. *Appl. Phys. Lett.* **123**, 022406 (2023).
14. Kostylev, M. P., Serga, A. A., Schneider, T., Leven, B. & Hillebrands, B. Spin-wave logical gates. *Appl. Phys. Lett.* **87**, 153501 (2005).
15. Chumak, A. V., Serga, A. A. & Hillebrands, B. Magnon transistor for all-magnon data processing. *Nature Commun.* **5**, 4700 (2014).
16. Fischer, T. et al. Experimental prototype of a spin-wave majority gate. *Appl. Phys. Lett.* **110**, 152401 (2017).
17. Talmelli, G. et al. Reconfigurable submicrometer spin-wave majority gate with electrical transducers. *Sci. Adv.* **6**, eabb4042 (2020).
18. Yu, W., Lan, J. & Xiao, J. Magnetic logic gate based on polarized spin waves. *Phys. Rev. Appl.* **13**, 024055 (2020).
19. Zhang, Z. et al. Bias-free reconfigurable magnonic phase shifter based on a spin-current controlled ferromagnetic resonator. *J. Phys. D: Appl. Phys.* **53**, 105002 (2019).
20. Lake, S. R., Divinskiy, B., Schmidt, G., Demokritov, S. O. & Demidov, V. E. Microscopic nonlinear magnonic phase shifters based on ultrathin films of a magnetic insulator. *Appl. Phys. Lett.* **121**, 052403 (2022).
21. Vogt, K. et al. Realization of a spin-wave multiplexer. *Nature Commun.* **5**, 3727 (2014).
22. Wang, Q. et al. Reconfigurable nanoscale spin-wave directional coupler. *Sci. Adv.* **4**, e1701517 (2018).
23. Zhang, Z. et al. Spin-wave frequency division multiplexing in an yttrium iron garnet microstripe magnetized by inhomogeneous field. *Appl. Phys. Lett.* **115**, 232402 (2019).
24. Sarker, M. S., Nakamura, S., Yamahara, H., Seki, M. & Tabata, H. Multifrequency spin-wave propagation for parallel data processing using microstructured yttrium iron garnet thin films. *IEEE Trans. Magn.* **58**, 4300706 (2022).
25. Serha, R. O. et al. Low-damping spin-wave transmission in yig/pt-interfaced structures. *Adv. Mater. Inter.* **9**, 2201323 (2022).
26. Casulleras, S. et al. Generation of spin-wave pulses by inverse design. *Phys. Rev. Appl.* **19**, 064085 (2023).
27. Divinskiy, B. et al. Dispersionless propagation of ultrashort spin-wave pulses in ultrathin yttrium iron garnet waveguides. *Phys. Rev. Appl.* **16**, 024028 (2021).
28. Schultheiss, K. et al. Time refraction of spin waves. *Phys. Rev. Lett.* **126**, 137201 (2021).
29. Muralidhar, S. et al. Femtosecond laser pulse driven caustic spin wave beams. *Phys. Rev. Lett.* **126**, 037204 (2021).
30. Merbouche, H. et al. Giant nonlinear self-phase modulation of large-amplitude spin waves in microscopic yig waveguides. *Sci. Rep.* **12**, 7246 (2022).
31. Sebastian, T., Schultheiss, K., Oby, B., Hillebrands, B. & Schultheiss, H. Micro-focused brillouin light scattering: imaging spin waves at the nanoscale. *Front. Phys.* **3**, 35 (2015).
32. Körber, L. et al. Pattern recognition in reciprocal space with a magnon-scattering reservoir. *Nature Commun.* **14**, 3954 (2023).
33. Covington, M., Crawford, T. M. & Parker, G. J. Time-resolved measurement of propagating spin waves in ferromagnetic thin films. *Phys. Rev. Lett.* **89**, 237202 (2002).
34. Sekiguchi, K. et al. Nonreciprocal emission of spin-wave packet in feni film. *Appl. Phys. Lett.* **97**, 022508 (2010).
35. Jamali, M., Kwon, J. H., Seo, S.-M., Lee, K.-J. & Yang, H. Spin wave nonreciprocity for logic device applications. *Sci. Rep.* **3**, 3160 (2013).
36. Suhl, H. The theory of ferromagnetic resonance at high signal powers. *J. Phys. Chem. Solids* **1**, 209 (1957).
37. Sushruth, M. et al. Electrical spectroscopy of forward volume spin waves in perpendicularly magnetized materials. *Phys. Rev. Research* **2**, 043203 (2020).
38. Mohseni, M. et al. Backscattering immunity of dipole-exchange magnetostatic surface spin waves. *Phys. Rev. Lett.* **122**, 197201 (2019).
39. Schultheiss, H., Vogt, K. & Hillebrands, B. Direct observation of nonlinear four-magnon scattering in spin-wave microconduits. *Phys. Rev. B* **86**, 054414 (2012).
40. Liu, H. J. J., Riley, G. A., Ordóñez Romero, C. L., Kalinikos, B. A. & Buchanan, K. S. Time-resolved study of nonlinear three-magnon processes in yttrium iron garnet films. *Phys. Rev. B* **99**, 024429 (2019).
41. Lendinez, S. et al. Nonlinear multi-magnon scattering in artificial spin ice. *Nature Commun.* **14**, 3419 (2023).
42. Hayashi, H. & Ando, K. Spin pumping driven by magnon polarons. *Phys. Rev. Lett.* **121**, 237202 (2018).
43. Sheng, L. et al. Nonlocal detection of interlayer three-magnon coupling. *Phys. Rev. Lett.* **130**, 046701 (2023).
44. Synogach, V. T., Fetisov, Y. K., Mathieu, C. & Patton, C. E. Ultrashort microwave pulses generated due to three magnon interactions. *Phys. Rev. Lett.* **85**, 2184–2187 (2000).
45. Mathieu, C., Synogach, V. T. & Patton, C. E. Brillouin light scattering analysis of three-magnon splitting processes in yttrium iron garnet films. *Phys. Rev. B* **67**, 104402 (2003).
46. Ordóñez Romero, C. L. et al. Three-magnon splitting and confluence processes for spin-wave excitations in yttrium iron garnet films: Wave vector selective brillouin light scattering measurements and analysis. *Phys. Rev. B* **79**, 144428 (2009).
47. Qu, T., Hamill, A., Victora, R. H. & Crowell, P. A. Oscillations and confluence in three-magnon scattering of ferromagnetic resonance. *Phys. Rev. B* **107**, L060401 (2023).
48. Makiuchi, T. et al. Persistent magnetic coherence in magnets. *Nature Mater.* **23**, 627–632 (2024).
49. Li, Y. et al. Hybrid magnonics: physics, circuits and applications for coherent information processing. *J. Appl. Phys.* **128**, 130902 (2020).

Acknowledgements

The work was supported by the U.S. DOE, Office of Science, Basic Energy Sciences, Materials Sciences and Engineering Division, with the device design, and sample fabrication and characterization supported under contract No. DE-SC0022060. D.B. acknowledges support by the U.S. National Science Foundation (NSF) under Grant No. DMR-2338060. W. Z. acknowledges support from AFOSR under award number FA2386-21-1-4091 and the U.S. NSF under Grant No. ECCS-2246254. Use of the Center for Nanoscale Materials (CNM), an Office of Science user facility, was supported by the U.S. Department of Energy, Office of Science, Office of Basic Energy Sciences, under Contract No. DE-AC02-06CH11357. K.-J.K. is supported by KAIST-funded Global Singularity Research Program for 2021 and the National Research Foundation of Korea (NRF) funded by the Korean Government (MSIP) under grant RS-2023-00275259, RS-2023-00207732. M.S. was supported by the education and training program of the Quantum Information Research Support Center, funded through the NRF by the Ministry of Science and ICT (MSIT) of the Korean government under grant No. 2021M3H3A103657313.

Author contributions

M.S. and Y. L. conducted the experiments and prepared all the figures. R.D. assisted the device fabrication. J.L., W.Z., and D.A.B. analyzed the results. M.S., A.H., K.J.K., V.N., and Y.L. conceived the idea. All authors reviewed the manuscript.

Competing interests

The authors declare no competing interests.

Additional information

Correspondence and requests for materials should be addressed to Axel Hoffmann, Kab-Jin Kim, Valentine Novosad or Yi Li.

Reprints and permissions information is available at <http://www.nature.com/reprints>

Publisher's note Springer Nature remains neutral with regard to jurisdictional claims in published maps and institutional affiliations.

Open Access This article is licensed under a Creative Commons Attribution 4.0 International License, which permits use, sharing, adaptation, distribution and reproduction in any medium or format, as long as you give appropriate credit to the original author(s) and the source, provide a link to the Creative Commons licence, and indicate if changes were made. The images or other third party material in this article are included in the article's Creative Commons licence, unless indicated otherwise in a credit line to the material. If material is not included in the article's Creative Commons licence and your intended use is not permitted by statutory regulation or exceeds the permitted use, you will need to obtain permission directly from the copyright holder. To view a copy of this licence, visit <http://creativecommons.org/licenses/by/4.0/>.

© UChicago Argonne, LLC, Operator of Argonne National Laboratory 2025